A MODEL FOR LIQUID PHASE SINTERING

J. SVOBODA†, H. RIEDEL and R. GAEBEL

Fraunhofer-Institut für Werkstoffmechanik, Wöhlerstraße 11, 79108 Freiburg, Germany

Abstract—A quantitative model for liquid phase sintering is developed based on the following ideas. During heating a liquid phase forms, which is easily mobile, wets the solid particles completely, dissolves solid atoms and provides an easy diffusion path for them. The solid density increases by particle rearrangement and by the flattening of particle contacts. Driving (or retarding) forces result from capillary stresses, from applied mechanical stresses, from the pressure of gas entrapped in closed pores and from differences in chemical potential of the dissolved and precipitated matter. At higher densities the driving force may become very small, since the liquid pressure decreases and a negative contribution from the solid–liquid interface energy increases. At this stage grain coarsening plays an important role for the continued filling of larger and larger pores. The model is applied to describe nonisothermal densification curves measured on Si_3N_4 for various hold temperatures, axial stresses and green densities. Adjusting a moderate number of parameters all having a physical meaning leads to good agreement between theory and experiment.

Copyright © 1996 Acta Metallurgica Inc. Open access under CC BY-NC-ND license.

1. INTRODUCTION

Liquid phase sintering is the consolidation of powder compacts with the aid of a liquid phase forming at temperatures well below the melting point of the base material. In this paper we consider brittle refractory base materials, such as silicon-nitride or tungsten carbide, which are pressed at room temperature to relative densities of typically 55% and sintered to full density with the aid of sinter additives such as oxides or metallic cobalt, respectively.

The present paper is an attempt to integrate the knowledge on the mechanisms of liquid phase sintering [1–5] into a comprehensive quantitative model. Such a constitutive model is needed for describing the sintering of parts with an inhomogeneous green density distribution using the finite element method [6–8]. The model comprises the following aspects: (i) primary rearrangement of the solid particles when the liquid phase is formed; (ii) grain shape accommodation by contact flattening [1]; and (iii) filling of large pores and grain coarsening in the final sintering stage [9–11]. These processes are not modeled as sequential events. Rather the model is formulated such that all mechanisms can act simultaneously in principle. Rearrangement dominates in the first sintering stage, shape accommodation in the second, and filling of large pores and grain coarsening in the third.

An important feature of the present model is that a pore size distribution is taken into account. Its primary effect is on the liquid pressure, which

constitutes the main part of the driving force for densification. The pores are filled consecutively beginning with the smallest. Since the liquid pressure is determined by the curvature of the pore surface, the liquid pressure decreases gradually as small pores are eliminated. This effect becomes particularly important in the late stages when only large pores remain unfilled.

The model is formulated in terms of the state variables solid volume fraction (also called relative solid density), D_s, flattening strain, δ, grain radius, R, and the liquid volume fraction in relation to the volume of the condensed matter (solid and liquid), g. The liquid fraction is assumed to be a function of the temperature only, and the grain radius obeys the usual laws for grain coarsening (Section 4.3). For δ an evolution equation is derived along the lines proposed by Kingery [1], and the evolution law for the solid volume fraction is written as

$$\dot{D}_s = \dot{D}_s^{(r)} + \dot{D}_s^{(m)} + \dot{D}_s^{(f)}. \tag{1}$$

The dot denotes the time derivative, and the superscripts indicate contributions by rearrangement (r), melting of additive particles (m) and contact flattening (f).

In the following three sections the evolution equations for the state variables are derived. A summary of the relevant equations is given in Section 5, while Section 6 gives a few examples of how the model describes the interplay between the densification mechanisms in relation to experiments on silicon-nitride.

---

†Permanent address: Academy of Sciences of the Czech Republic, Zizkova 22, Brno, Czech Republic.

2. REARRANGEMENT

2.1. Driving force and transport mechanism

To describe particle rearrangement we make the plausible assumption that rearrangement processes can lead to a certain maximum density of the solid phase, denoted by D_1. For spherical particles, D_1 corresponds to the density of the random dense sphere packing, $D_1 = 0.63$. Higher solid densities cannot be reached by rearrangement alone.

The driving forces for rearrangement are the capillary forces exerted on the solid particles by the liquid and a possibly applied mechanical pressure. When the solid density, D_s, is equal to D_1, the driving forces are balanced, and the particle packing is in a state of equilibrium. If $D_s < D_1$, however, a net driving force for rearrangement and densification results from unbalanced forces. Hence we assume that the densification rate of the solid phase by rearrangement is proportional to the same force that drives contact flattening, multiplied by $(D_1 - D_s)$.

Rearrangement requires the sliding of the solid particles against one another with a lubricating liquid film between the particles. Hence the densification rate of the solid phase by rearrangement should depend on the viscosity of the liquid, η, on the liquid film thickness, δ_b, and on the area of the particle contacts, πc^2, in the following way

$$\dot{D}_s^{(r)} = bD_s \frac{\delta_b R}{\eta c^2} (\sigma_s - \sigma_m)(D_1 - D_s) \qquad (2)$$

if $D_1 > D_s$; otherwise $\dot{D}_s^{(r)} = 0$. Here R is the radius of the solid particles, σ_s is the sintering stress defined in equation (22) below, σ_m is the mean stress acting on the material (i.e. the negative mechanical pressure), c is the contact radius, which increases by contact flattening as described in Section 3, and b is a dimensionless factor. In this paper $b = 1$ is used arbitrarily, since the precise value of η is not known anyway. The liquid film thickness is assumed to be the equilibrium film thickness [12], $\delta_b \approx 1.5$ nm.

If the liquid fraction exceeds $1 - D_1$ ($= 0.37$ for spherical particles), the material can be densified completely by rearrangement alone. Contact flattening may accompany rearrangement, but it is not necessary for complete densification. However, in the systems that are of primary interest in this paper, the liquid fractions are much lower than 37%, so that grain shape accommodation is necessary.

2.2. Melting of additive particles

The immediate effect of melting is to reduce the solid density according to

$$\dot{D}_s^{(m)} = -\frac{\dot{g}}{1 - g} D_s \qquad (3)$$

($g = $ current liquid fraction). However, the disappearance of additive particles and the partial solution of the base material in the melt opens the possibility for rearrangement of the remaining solid particles

according to equation (2), so that the total density increases. If the additive particles are substantially larger than the particles of the base material, their melting may leave large pores, which are not immediately filled by rearrangement. This possibility is accounted for by assuming the presence of a volume fraction of large pores, f_{c0}, which play a role in the final sintering stage.

3. SHAPE ACCOMMODATION BY CONTACT FLATTENING

Under the action of the capillary forces and of a possibly applied compressive force, particles tend to develop flattened contacts and the particle centers approach one another. Solid matter is dissolved in the liquid within the contacts, and deposited on the particle surface outside the contacts. The rate controlling step may either be the surface reaction of solution/precipitation or the diffusive transport of the solid species along the liquid film. These problems were first analyzed by Kingery [1] and later by several other groups [13–15].

In the present paper we develop an analytical solution which comprises both limiting cases of reaction and diffusion control. Since the analytical solution is strictly valid only for small contacts, a more general numerical solution is also presented, which shows that the range of validity of the analytical solution is rather large.

3.1. Geometry

Figure 1 shows the geometry of the model analysed in this section. Initially spherical particles with radius R develop circular solid contacts with radius c. Their center-to-center spacing is $2R(1 - \delta)$, where δ is called the flattening strain. An axisymmetric unit cell is considered comprising $1/Z$ of a particle, where Z is the coordination number (i.e. the average number of contacts of a particle to its neighbors). Hence the opening angle of the unit cell is given by

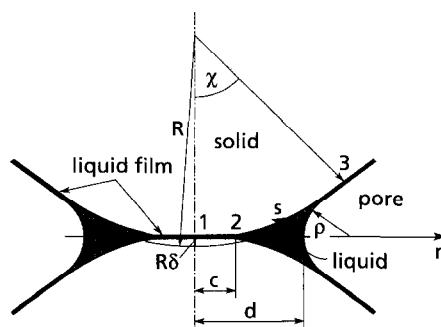$$\cos \chi = 1 - \frac{2}{Z}. \qquad (4)$$

Fig. 1. Geometry of an axisymmetric neck with a liquid collar. The solid–liquid interface merges into the contact with dihedral angle $\psi = 0$.

Like Kingery [1] we assume that the solid is fully wetted by the liquid. As a consequence the dihedral angle at the solid–solid contact and the wetting angle are zero, and the grains are covered with an atomically thin liquid film.

The equilibrium shape of the liquid surface in Fig. 1 is given by a Delaunay arc [16] and is called a nodoid [4]. The shape is approximated by a circular arc with radius ρ in the present paper, since the difference is vanishingly small.

The densification rate of the solid phase due to contact flattening is given by

$$\dot{D}_s^{(f)} = \frac{3D_s\dot{\delta}}{(1 - \delta)}. \tag{5}$$

The rate, $\dot{\delta}$, will be derived.

3.2. Pore size distribution and liquid pressure

The liquid phase is assumed to be easily mobile throughout the whole powder compact. Therefore in equilibrium the liquid pressure and hence the mean surface curvature of the liquid surface must be uniform. To establish a uniform curvature, the liquid fraction in the neck between a pair of small particles must be greater than that between two large particles. This variable amount of liquid fraction in different necks has a large effect on the evolution of the liquid pressure, as will be shown next. Otherwise its effect on the rate of contact flattening is small, as we shall see in the numerical model.

The situation shown in Fig. 1 is that of an isolated liquid collar around the solid neck. A new situation arises when, upon further densification, the liquid meniscus reaches the boundary of the unit cell (point 3 in Fig. 1). This is a critical state at which the pore channel surrounding the neck is instantaneously filled with liquid, for the following reason. Up to the critical point the curvature of the liquid surface decreases when an incremental amount of liquid is added to the neck from the surrounding material, which can be regarded as an infinite reservoir. After the critical point the curvature and hence the surface tension increase. The increasing surface tension cannot be balanced by the liquid pressure in the reservoir. Hence the supercritical neck attracts liquid until the pore channel is completely filled by the liquid. This is a loose analogy to the well-known case of connected soap bubbles. In this way the currently smallest pore is eliminated, and the liquid pressure is determined by the surface curvature of the smallest of the remaining pores, which is just in the critical state with the meniscus at point 3. Analogously the large isolated pores are filled in the final stage of sintering.

3.3. Governing equations

The hydrostatic pressure in the liquid is given by the liquid surface curvature. In the circular-arc approximation

$$p_l = -\gamma_l\left(\frac{1}{\rho} - \frac{1}{d}\right), \tag{6}$$

where γ_l is the specific surface energy of the liquid; d and ρ are defined in Fig. 1. The chemical potential of solid atoms in the solid is given by

$$\mu = -\Omega(\sigma_b - p_l) \quad \text{at the contact} \tag{7}$$

$$\mu = \Omega(p_l - 2\gamma_{sl}\kappa) \quad \text{at the solid–liquid interface} \tag{8}$$

$$\mu = -2\Omega(\gamma_{sl} + \gamma_l)\kappa \quad \text{at the solid surface.} \tag{9}$$

The chemical potential of solid atoms dissolved in the liquid is

$$\mu^* = kT \ln(C/C_e) + p_l\Omega. \tag{10}$$

Here Ω is the atomic volume of the dissolving species (assumed to be the same in the solid and in the liquid), σ_b is the mechanical stress transmitted between the solid grains across the contact (σ_b will be determined), γ_{sl} is the specific surface energy of the solid–liquid interface, κ is the mean curvature of that interface (being negative for a spherical solid particle, $\kappa = -1/R$), k is Boltzmann's constant, T is the absolute temperature, C is the concentration of solid atoms in the liquid, and C_e is the equilibrium concentration, if the liquid is in contact with a planar solid surface.

The normal displacement rate of the solid–liquid interface by solution/precipitation is given by

$$\dot{u}_n = L(\mu^* - \mu), \tag{11}$$

where L is the reaction rate constant for solution or precipitation; and $\dot{u}_n$ is positive when the solid grows. For the contact area this means, according to equations (7) and (10),

$$R\dot{\delta} = -L[\Omega\sigma_b + kT \ln(C/C_e)]. \tag{12}$$

The diffusion of dissolved solid atoms through the bulk liquid is assumed to be very fast, so that the chemical potential is uniform in the bulk liquid. Hence the rate of diffusion needs to be considered only where the liquid is present as an atomically thin film like in the particle contacts. The radial diffusive flux of solid atoms in the liquid contact film is given by Fick's first law

$$j = -\delta_b D_b \frac{dC}{dr}, \tag{13}$$

where D_b is the diffusion coefficient of the solid atoms in the liquid grain boundary and r is the radial coordinate from the center of the contact area. Mass conservation demands that

$$j = R\dot{\delta}r. \tag{14}$$

Equating the right-hand sides of equations (13) and (14) leads to the radial distribution of the concentration

$$C(r) = C_1 + \frac{R\dot{\delta}(c^2 - r^2)}{2\delta_b D_b},$$ (15)

where C_1 is the concentration in the liquid collar. In the liquid film on the grain surface the combination of equation (11) and Fick's second law gives

$$\delta_1 D_1\left(\frac{d^2 C}{ds^2} + \frac{1}{r}\frac{dr}{ds}\frac{dC}{ds}\right)$$

$$= L\left(kT\ln\frac{C}{C_e} + 2(\gamma_{sl} + \gamma_1)\Omega\kappa + p_1\Omega\right)$$ (16)

where δ_1 and D_1 are the thickness of, and the diffusivity in, the liquid film on the particle surface, and s is the arc length along the particle surface (see Fig. 1).

3.4. Analytical solution

The flattening strain rate, $\dot{\delta}$, is now determined from the condition of mechanical equilibrium. From equation (12) one obtains

$$\sigma_b = -\frac{kT}{\Omega}\ln\frac{C}{C_e} - \frac{R\dot{\delta}}{L\Omega}.$$ (17)

The force exerted on the unit cell by σ_b is

$$F_b = 2\pi\int_0^c \sigma_b r\,dr$$

$$= \frac{2\pi kT\delta_b D_b}{\Omega R\dot{\delta}}\left[C_1\left(\ln\frac{C_1}{C_e} - 1\right)\right.$$

$$\left. - C_0\left(\ln\frac{C_0}{C_e} - 1\right)\right] - \pi c^2\frac{R\dot{\delta}}{L\Omega}$$

$$\approx -\pi c^2\left(\frac{1}{L\Omega} + \frac{kTc^2}{4C_1\Omega\delta_b D_b}\right)R\dot{\delta}$$

$$- \pi c^2\frac{kT}{\Omega}\ln\frac{C_1}{C_e}$$ (18)

where C_0 is the concentration of solid atoms in the liquid in the center of the contact, i.e. for $r = 0$ in equation (15). The third line of equation (18) follows from the second by a series expansion for small $(C_0 - C_1)/C_1$. Although this quantity is not necessarily small, the expansion does not cause a large error, and we continue using the linearized form.

The force exerted by the liquid on the unit cell is

$$F_1 = -\pi d^2 p_1 + 2\pi d\gamma_1,$$ (19)

where the second term is the surface tension force. Mechanical isostatic forces correspond to the force on the unit cell [17]

$$F_{ex} = \frac{4\pi R^2\sigma_m}{D_s Z(1 - \delta)},$$ (20)

where σ_m is the mechanical mean stress. If a gas is entrapped in the pore space, the difference, Δp, between the pressure in the pores and the external gas pressure must be added to σ_m (see Section 4.4). The equilibrium condition $F_b + F_1 = F_{ex}$ leads to the flattening strain rate

$$\dot{\delta} = \frac{4R}{ZD_s(1 - \delta)}\frac{\sigma_s - \sigma_m - \Delta p}{c^2/(L\Omega) + kTc^4/(4C_1\Omega\delta_b D_b)}.$$ (21)

The effects of the liquid pressure, of the solid–liquid interface energy and of chemical forces are summarized in a sintering stress, σ_s

$$\sigma_s = \sigma_1 + \sigma_{sl} + \sigma_\mu.$$ (22)

Expressions for the effective liquid pressure, σ_1, and for the contribution of the solid–liquid interface energy, σ_{sl}, are given next, while the effective chemical pressure, σ_μ, will be considered in Section 3.5. The grain radius increases according to equation (36); coarsening alone does not change δ, since it is assumed to occur in a self-similar manner.

The influence of the liquid forces is summarized in the effective liquid pressure

$$\sigma_1 = \frac{\gamma_1(d^2/\rho + d)ZD_s(1 - \delta)}{4R^2}.$$ (23)

The relationship between σ_1 and p_1 can be obtained by comparing equations (6) and (23). The quantities d and ρ can be expressed by the liquid fraction and the particle displacement. These geometrical relations are relatively complicated, but it turns out that the effective liquid pressure is not sensitive to the amount of liquid nor to the density. For $Z = 8$, σ_1 can be approximated by the simple formula

$$\sigma_1 = \frac{3\gamma_1}{R}$$ (24)

which is used for calculating the analytical results shown in Figs 4 and 5 below. In Section 4, equation (24) will be modified to account for the presence of large pores.

The contribution of the solid–liquid interface energy to the sintering stress is

$$\sigma_{sl} = -\frac{kTZD_s(1 - \delta)c^2}{4\Omega R^2}\ln\frac{C_1}{C_e}.$$ (25)

As long as the contacts are relatively small, the chemical potential is determined by the equilibrium of the liquid with the curved particle surface characterized by the grain radius R. Equations (8) and (10) give the concentration $kT\ln(C_1/C_e) = 2\gamma_{sl}\Omega/R$. Hence σ_{sl} becomes

$$\sigma_{sl} = -\frac{Z}{2}D_s(1 - \delta)\frac{c^2}{R^2}\frac{\gamma_{sl}}{R}.$$ (26)

This contribution to the sintering stress is negative and its amount increases with increasing contact radius. Since σ_{sl} is important primarily in the final sintering stage, the small-contact approximation,

equation (26), will be replaced in Section 4 by an expression appropriate for the later sintering stages.

Kingery [1] expresses the contact radius c by the geometrically motivated relation

$$c^2 = 2R^2\delta. \tag{27}$$

In the Appendix we show that this equation is asymptotically exact for small c/R. A comparison with the numerical solution in Section 3.6 shows that it is also reasonably accurate for larger c/R.

With Kingery's expression for c^2, equation (21) can be integrated, and one obtains

$$\delta^2 + \frac{kTR^2L}{3C_1\delta_bD_b}\delta^3 = \frac{4L\Omega}{ZD_sR}(\sigma_s - \sigma_m)t, \tag{28}$$

where δ and $(c/R)^2$ are neglected compared to unity and the grain size is kept constant. For small times, the first term on the left-hand side dominates, so that $\delta \propto t^{1/2}$ and $c \propto t^{1/4}$. This is the limiting case of reaction control. For slow diffusion the second term starts to dominate after a short time, so that $\delta \propto t^{1/3}$ and $c \propto t^{1/6}$. This is the diffusion controlled case.

3.5. Chemical forces

In many systems the precipitated matter has a different chemical composition or a different lattice structure than the dissolved grains. In the following we will consider the dissolved and precipitated matter as different phases, α and β, although they need not be different phases in the thermodynamic sense. In the W/Ni system, for example, pure tungsten grains are inserted, while the precipitated material is a W–0.15 wt% Ni solid solution [2, 3, 18]. The difference in chemical potential between the precipitated β and the dissolved α phases is $\mu_\beta - \mu_\alpha$, which is usually negative. For simplicity we assume here that the reaction rate constant L, the surface energy, the atomic volume Ω, and the surface curvature of the two phases are equal. This is not always justified, but the effect of the chemical potential difference is brought out more clearly, if other possible differences are neglected. Other aspects of the analysis are approximate anyway.

Compared to the analysis with $\mu_\beta - \mu_\alpha = 0$ three changes are necessary. First, in the presence of two phases the concentration of solid atoms in the liquid is

$$kT \ln \frac{C_1}{C_c} = \frac{2\gamma_{sl}\Omega}{R} - a_\beta(\mu_\alpha - \mu_\beta), \tag{29}$$

instead of the equation preceding equation (26); C_c is still the concentration in equilibrium with phase α, and a_β is the surface area fraction of phase β in contact with the liquid.

Second, the chemical potentials in β grains are obtained by adding $\mu_\beta - \mu_\alpha$ in equations (7)–(9). This leads to different displacement rates for the three types of contacts, α–α, β–β and α–β. The α–α and

β–β contacts are obviously symmetric. The displacement rates on either side of an α–β contact differ by

$$\dot{u}_\alpha - \dot{u}_\beta = L(\mu_\alpha - \mu_\beta). \tag{30}$$

If $R\dot{\delta}$ is defined as the arithmetic mean of $\dot{u}_\alpha$ and $\dot{u}_\beta$, the final result for δ can be written in the form of equation (21) for all types of contacts with the effective chemical pressure

$$\sigma_\mu = A\frac{Z}{4}D_s(1-\delta)\frac{c^2}{R^2}\frac{\mu_\alpha - \mu_\beta}{\Omega}, \tag{31}$$

where the factor A is: $A = a_\beta$ for α–α contacts, $A = -(1 - a_\beta)$ for β–β contacts, and $A = a_\beta - 1/2$ for α–β contacts.

Third, the simple geometrically motivated relation $c^2 = 2R^2\delta$, equation (27), must be reconsidered. For β–β contacts, A is negative and hence the effective chemical pressure is negative. For very small contacts, the capillary stresses still dominate, since σ_1 is independent of c while $\sigma_\mu \propto c^2$. But since chemical forces are usually large compared to capillary forces, the (negative) chemical pressure starts to dominate soon and leads to swelling of the β–β contact, i.e. δ becomes negative. The shape evolution of the neck is influenced also by the material deposited on the β grains outside the neck, where the deposition rate is larger than in the contact.

The situation at the asymmetric α–β contact is even more complicated. Due to the proximity of the α phase, matter can be deposited on the β side of the contact faster than on the particle surface. This leads to the evolution of a hump on the β grain and a dip in the α grain. If the two grains are mechanically constrained from approaching one another, it appears possible that the liquid grain boundary detaches from the neck and traverses the α grain. Such a situation was observed in the W/Ni system by Huppmann *et al.* [18] and described by a two-dimensional numerical model by Nikolic and Huppmann [19].

Considering the complexity of these processes and the difficulty of determining the surface area fractions of the phases and the frequency of the three types of contacts, equation (31) can be used only as an order-of-magnitude estimate using plausible assumptions on the average value of A. In the following, cases without a chemical driving force are considered.

The difference in chemical potential also enhances the coarsening rate. For a representative grain covered with β phase, the growth rate becomes, instead of equation (36)

$$\dot{R} = \frac{\gamma_{sl}\Omega L}{4R} + (1 - a_\beta)L(\mu_\alpha - \mu_\beta). \tag{32}$$

3.6. Numerical solution

The equations for the precipitation rate, equation (11), and for diffusion along the liquid film on the particle surface, equation (16), are solved numerically

by replacing differentials by finite differences. On the grain boundary, the analytical solution, equations (14) and (15), is used. At each time step the displacement rates, $\dot{u}_n$, of the interfaces are calculated from the current values of the curvature and the chemical potential in the liquid. The position at the end of the time step follows from the position at the beginning of the time step and the velocity. A simple Euler forward integration method is used [20].

Computationally, the fulfilment of the equilibrium condition requires an iteration loop in each time step. One starts prescribing a certain concentration and zero flux at the boundary of the unit cell (point 3 in Fig. 1), integrates equations (11) and (16) numerically and thus obtains the flux out of the grain boundary and concentration C_1. This specifies $\dot{\delta}$ and σ_b. If the resulting σ_b is not in equilibrium with the liquid pressure and the applied pressure, a new value is chosen for the concentration at point 3 until the equilibrium condition is fulfilled.

Figure 2 shows the calculated evolution of a contact for the reaction controlled case (a) and for a primarily diffusion controlled case (b). In the case of reaction control, a strong curvature of the solid–liquid interface develops near the grain boundary. The radius of curvature at the neck tip is calculated in the Appendix to be approximately $c^2/(2R)$, which is equal to $R\delta$. This is consistent with the numerical result. In the case of diffusion control, no strong curvature is observed numerically and none is predicted analytically in the Appendix.

After the liquid meniscus reaches the boundary of the unit cell, it is fixed at this point in the numerical model, as Fig. 2 shows. Hence the liquid volume is not preserved in the unit cell. Consistently with Section 3.2 the excess liquid is assumed to fill the pore channels around other necks completely, because intermediate states between that shown in the figure and complete pore filling are unstable. Since the
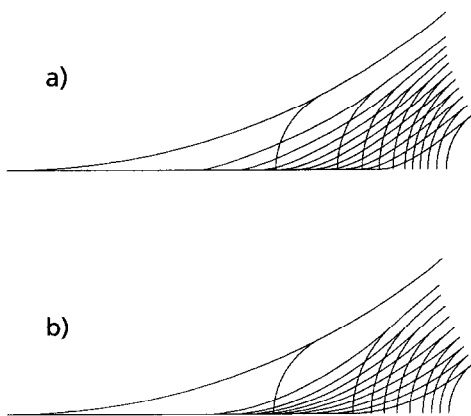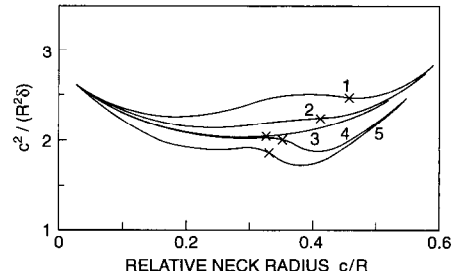

Fig. 3. Numerical results for $c^2/(R^2\delta)$ (for $Z = 8$). The numbers correspond to (1) $\hat{D} = \infty$, $g = 2\%$; (2) $\hat{D} = \infty$, $g = 5\%$; (3) $\hat{D} = \infty$, $g = 10\%$; (4) $\hat{D} = 0.002$, $g = 2\%$; (5) $\hat{D} = 0.002$, $g = 5\%$.

liquid pressure is uniform throughout the whole system, the behavior of the neck is the same no matter whether the meniscus is at the critical point or whether the pore channel is filled.

Figure 3 shows the ratio $c^2/(R^2\delta)$. For very small contacts the numerical method is not accurate enough to reproduce the asymptotic behavior $c^2/(R^2\delta) = 2$. It shows, however, that the asymptotic result can serve as a reasonable approximation for the whole range.

The approximation for the effective liquid pressure, $\sigma_1 \approx 3\gamma_1/R$, underestimates the numerical result by about 20% (Fig. 4). The crosses mark the point when the liquid meniscus reaches the boundary of the unit cell. Here the numerical result starts to rise. However, this increase is an artifact of the unit cell model, in which the curvature of the liquid surface increases after that critical point, as the space between grains shrinks during densification. In reality the pores exhibit a size distribution the smallest being filled first. Hence, as pointed out in Section 3.2 the liquid pressure is determined by larger and larger pores and therefore actually decreases.

Figure 5 shows the flattening strain as a function of the time. The analytical and numerical solutions are consistent in the whole time range. The numerical results confirm the independence of δ from the liquid fraction, at least in the considered range of 2–10%

Fig. 2. Evolution of the axisymmetric solid–liquid interface for $Z = 8$; (a) reaction control: $\hat{D} \equiv C_e D_b \delta_b/(LkTR^2) = \infty$, time between plotted states $\Delta t = 0.011\hat{t}$ with $\hat{t} = R^2/(\Omega\gamma_1 L)$, time to full densification $t_f = 0.001\hat{t}$; (b) primarily diffusion controlled case: $\hat{D} = 0.002$, $\Delta t = 0.01\hat{t}$, $t_f = 0.097\hat{t}$.
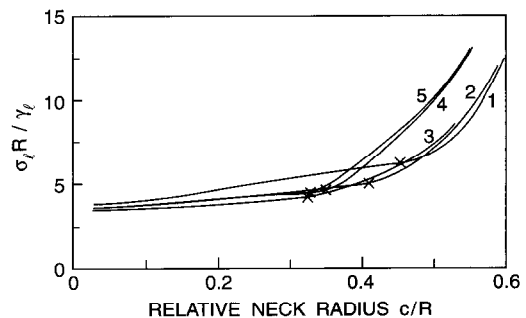

Fig. 4. Effective liquid pressure as a function of the normalized neck radius. Curves numbered as in Fig. 3.
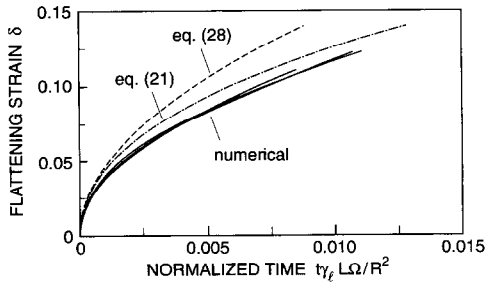
Fig. 5. Evolution of the flattening strain δ in the reaction controlled case. Numerical results for $g = 2$, 5 and 10%. Analytical results from equations (21) or (28).

liquid. Also Gessinger et al. [13] find only a small influence of the liquid fraction numerically.

4. PROCESSES DOMINATING IN THE FINAL SINTERING STAGE

In the final sintering stage, contact flattening continues, and we use the same equation as previously to describe it, equation (21). However, the relative importance of the liquid pressure, of the solid–liquid interface energy and of grain coarsening changes substantially compared to the intermediate stage, and a gas pressure can build up after pore closure. Whereas the contribution of the solid–liquid interface energy to the sintering stress is negligible compared to the liquid pressure in the intermediate stage, it gains a dominant importance in the final stage, since its amount increases while the liquid pressure drops, so that at a certain stage the two may balance one another. Now grain coarsening becomes the rate controlling process, since it reduces the (negative) contribution of the solid–liquid interface energy to the sintering stress, so that a small driving force for densification is maintained, as the grains grow. The equations describing this idea are explained next.

4.1. The effective liquid pressure

As pointed out previously, the liquid pressure is controlled by the smallest of the remaining large pores. Hence the liquid pressure decreases when the porosity decreases and ever larger pores remain unfilled. This is described phenomenologically by

$$\sigma_1 = \text{Min}\left(\frac{3\gamma_1}{R}, \frac{3\gamma_1}{R_0}\left(B + (1 - B)\left(\frac{f}{f_{c0}}\right)^n\right)\right), \quad (33)$$

where f is the porosity calculated as

$$f = 1 - \frac{D_s}{1 - g}, \quad (34)$$

f_{c0} is the volume fraction of large pores at the beginning of the final stage, and B and n are adjustable parameters. "Large pores" are pores

having a size larger than $2R/3$, because these pores remain unfilled at the effective liquid pressure $3\gamma_1/R$. Since the grain size grows, the number of pores considered as being large decreases. The functional form of σ_1 reflects the size distribution of the large pores in a way not specified here.

4.2. The contribution of the solid–liquid interface energy to the sintering stress

Since the contribution of the solid–liquid interface energy to the sintering stress becomes important in the final sintering stage, we replace the small-contact approximation, equation (26), by

$$\sigma_{sl} = -\left(\frac{0.5}{\sqrt{1 - D_s}} - 0.884\right)\frac{\gamma_{sl}}{R}. \quad (35)$$

This describes the contribution of the solid–liquid interface energy to the sintering stress when the solid–liquid interface has an equilibrium shape. The expression is adjusted to the numerical results developed in Ref. [21] for the dihedral angle $\psi = 0$, and it also approximates equation (26) for small contacts.

4.3. Grain coarsening

Grain coarsening in the presence of a liquid phase is a complicated process, which is called Ostwald ripening, if the solid particles are dispersed in the liquid phase, or grain growth by grain boundary migration, if the solid phase forms a dense polyhedral grain structure. Grain boundary migration means that solid atoms are dissolved on one side of the boundary, transported across the thin liquid film and deposited on the other side of the boundary.

In keeping with our previous assumption we assume that diffusion through the bulk liquid is fast, so that the rate of grain coarsening is reaction controlled. In this case the grain growth rate obeys the same kinetic law for Ostwald ripening and for boundary migration. The common form of the evolution equation for the grain radius is

$$\dot{R} = \frac{\gamma_{sl}L\Omega}{4R} \quad (36)$$

which is used here for all sintering stages. The equations describing the flattening mechanism were deliberately formulated in such a way that the structure coarsens in a self-similar manner, if densification is suppressed by some intervention mechanism, i.e. δ is not changed by coarsening alone. Integration of equation (36) for constant L gives

$$R^2 - R_0^2 = \frac{\gamma_{sl}L\Omega}{2}t \quad (37)$$

with the initial grain radius R_0. Experimental results supporting equation (37) are given by Lee et al. [22].

4.4. Gas pressure in isolated pores

After pore closure the gas entrapped in the isolated pores is compressed when the pores shrink. The evolving gas pressure depends on whether and how fast the gas can escape from the pores by dissolving in the material. In the example calculations shown in Section 6 we make one of two extreme assumptions: (i) the gas pressure is the equilibrium vapor pressure (which is negligible for Si_3N_4 below 1700°C); and (ii) the gas is firmly entrapped in the pores.

In the case of firmly entrapped gas, the pressure is given by the current pore volume and the temperature, both in relation to their values in the moment of pore closure. Thus for an ideal gas the pressure difference between the pores and the furnace atmosphere is

$$\Delta p = p_{ex,cl} \frac{f_{cl}}{f} \frac{1-f}{1-f_{cl}} \frac{T}{T_{cl}} - p_{ex} \qquad (38)$$

for $f < f_{cl}$; $\Delta p = 0$ for $f > f_{cl}$. Here p_{ex} is the external gas pressure. The subscript cl denotes the values of pressure, temperature and porosity at pore closure. The porosity at pore closure can be estimated from the results of Ref. [21]. In the presence of enough liquid phase the surface of the pore space corresponds to the case where the dihedral angle is $\psi = 90°$. For a coordination number $Z = 8$ and $\psi = 90°$, the porosity at pore closure is $f_{cl} = 12.5\%$ according to Ref. [21]. This value is used in the numerical examples.

5. SUMMARY OF THE ANALYTICAL MODEL

The analytical model now consists of evolution equations for the three state variables D_s, δ and R and a number of auxiliary equations. The liquid fraction, g, is assumed to be prescribed, for example as a function of the temperature, which in turn is prescribed as a function of the time. In the same way the material parameters η, $\delta_b D_b$, L, $C_l(\approx C_e)$, γ_{sl}, γ_l and Ω are prescribed. The mechanical stress σ_m and the external pressure p_{ex} are given as a function of time. The coordination number can either be fixed at the representative value $Z = 8$, or one of the semi-empirical relations proposed in Refs [23, 24] can be used, e.g. $Z = 12D_s$. Further parameters are b (set to 1 here), D_l, f_{co}, n and B (set to 0.07). The starting conditions for $t = 0$ are $D_s = D_0$ (= relative green density), $R = R_0$ and $\delta = 0$. Chemical forces are ignored here.

The integration of the coupled evolution equations (1), (21) and (36) usually requires numerical methods. A simple Euler forward algorithm is used. In each time step the right-hand sides of the evolution equations are calculated in the following way.

Porosity f from (34), contact radius c from (27), effective liquid pressure σ_l from (33), σ_{sl} from (35), sintering stress σ_s from (22), gas pressure difference from (38), densification rate by contact flattening $\dot{D}_s^{(f)}$

from (5), densification rate by melting $\dot{D}_s^{(m)}$ from (3), densification rate by rearrangement $\dot{D}_s^{(r)}$ from (2).

This specifies the rates of the state variables and their change during the time step. The state variables are updated and one proceeds to the next time step until the desired density is reached. The relative density is calculated from

$$D = 1 - f = \frac{D_s}{1-g}. \qquad (39)$$

Computing times for typical sintering cycles are a few seconds on a 486 personal computer. Examples are shown next in comparison with experimental results.

6. COMPARISON WITH EXPERIMENTS

A silicon-nitride powder (Bayer gas-phase powder) with 7.5 wt% of the spinel Al_2MgO_4 as a sintering additive was used to test the model. The initial mean grain size was 0.44 μm, and the phase content of the silicon-nitride was 93% α phase and 7% β phase. The theoretical density is assumed to be 3.17 g/cm³. Cylindrical powder compacts with 16 mm diameter and 13.5–15 mm height were pressed in a die at room temperature. An axial pressure of 150 MPa yielded a green density $D_0 = 0.57$. Green compacts with $D_0 = 0.503$ and 0.462 were also produced using axial pressures below 10 MPa. The powder compacts were either freely sintered or sintered under a uniaxial compressive stress (sinter forging [25, 26]) in a hot press. A nitrogen pressure $p_{ex} = 0.7$ MPa was applied. X-ray studies showed that the α-to-β phase transformation only started in the intermediate to late stages and supposedly did not influence the densification to a large extent. Axial and radial strain rates were recorded during sinter forging. Further details will be published elsewhere [27].

The model summarized in the preceding section was adjusted to measure densification curves. Since all parameters play a transparent role in the model, the adjustment could be done by hand without the aid of a numerical fit routine. No effort was made to achieve a perfect fit. The results shown in the diagrams below were calculated using the following material parameters and properties. Initial grain radius $R_0 = 0.22$ μm. The liquid fraction is estimated from X-ray studies showing that the crystalline sinter additives start to disappear at about 1200–1300°C to form a liquid phase. This process is spread out over a wide temperature range. The maximum liquid fraction is about 9% at 1700°C according to the powder producer. All this is described by

$$g = 2 \times 10^{-4}(T - 1508) \qquad (40)$$

for 1508 K $< T <$ 1973 K, and $\dot{g} = 0$ outside this range. Other material parameters are obtained by

adjusting the calculated densification curves to the experiments. These are

$$L\Omega = 2 \times 10^{11} \exp\left(-\frac{1024 \text{ kJ/mol}}{R_g T}\right) \frac{m^3}{Ns} \quad (41)$$

$$lC_l\Omega\delta_h D_h = 7 \times 10^{-35} \exp\left(-\frac{663 \text{ kJ/mol}}{R_g T}\right) \frac{m^6}{s} \quad (42)$$

$$b\delta_h/\eta = 40 \exp\left(-\frac{663 \text{ kJ/mol}}{R_g T}\right) \frac{m^3}{Ns} \quad (43)$$

$$\gamma_{sl} = \gamma_l = 0.5 \text{ J/m}^2. \quad (44)$$

Here R_g is the gas constant. To limit the number of adjustable parameters the two activation energies for diffusion and for the viscosity, and the two surface energies were not adjusted separately, but were given common values.

A last group of parameters, D_1, f_{c0}, n and B, is considered to depend on the green density. The density achievable by rearrangement, D_1, was chosen as

$$D_1 = D_0 + 0.06 \quad (45)$$

in order to fit the experimental densification curves. Most of the green compacts had $D_0 = 0.57$, so that in this case $D_1 = 0.63$ is the density of the random dense sphere packing. The volume fraction of large pores was chosen as $f_{c0} = 0.3$, 0.33 and 0.36 for $D_0 = 0.57$, 0.503 and 0.462, respectively. The corresponding values of n were 1.0, 1.0 and 3.0; $B = 0.07$ was used throughout.

Figure 6 shows measured and calculated densification curves for different hold temperatures (1550–1700°C). In all cases the heating rate was 30 K/min.

Fig. 7. Theoretical (dashed lines) and experimental (solid lines) densification curves for axial stresses $\sigma_z = 0$, -3.3 and -5.4 MPa (bottom to top), corresponding to mean stresses $\sigma_m = \sigma_z/3 = 0$, -1.1 and -1.8 MPa, respectively.

The time is set to zero when melting starts at 1235°C. Since the role of entrapped gas is not clear *a priori*, the calculation was carried out both with Δp from equation (38), and without a gas pressure $\Delta p = 0$. The difference is visible only at high density.

Figure 7 shows the dependence of the sintering curves on the axial stress for hold temperature 1700°C. Only the case without gas pressure is shown for clarity. The error bar indicates the experimental scatter among three nominally identical tests. Densities measured in interrupted tests (symbols in Fig. 7) are consistent with the values obtained from the axial and radial extensometers during the sinter forging test (solid lines).

Figure 8 shows the dependence of the sintering behavior on the green density. The slow densification rate of poorly densified green bodies is described in the model by a larger volume fraction of large pores and by the associated steeper decrease of the effective liquid pressure with density ($n = 3$ for $D_0 = 0.452$ vs $n = 1$ for $D_0 = 0.57$).
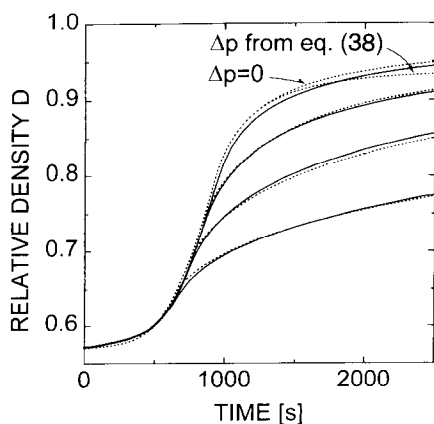

Fig. 6. Densification curves for hold temperatures 1550, 1600, 1650 and 1700°C (bottom to top). Comparison of theoretical (dashed lines) and experimental (solid lines) results. The parameters are given in the text.
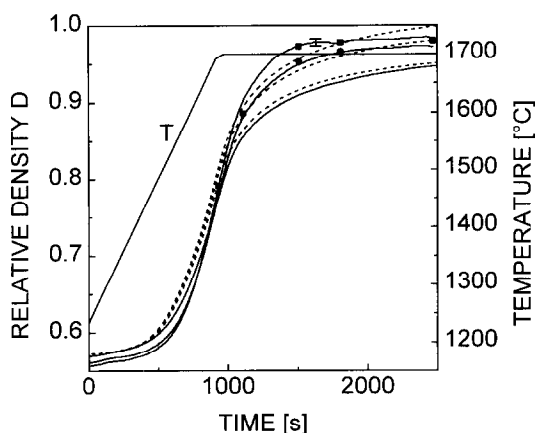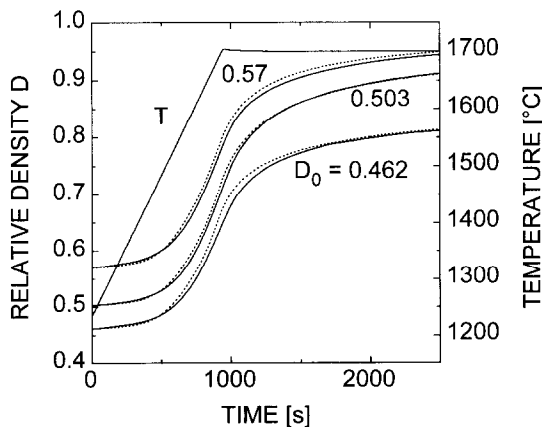

Fig. 8. Densification curves for various green densities $D_0 = 0.57$, 0.503 and 0.462.

7. DISCUSSION

To simulate densification curves for free sintering at various hold temperatures (Fig. 6) and their stress dependence (Fig. 7) seven parameters were adjusted, five of them for the reaction and transport coefficients including their temperature dependences, one for the interface energies, and one for the volume fraction of large pores. All other model parameters were prescribed rather than fitted to the experiments. The values of the activation energies and of the interface energies resulting from the fit have a reasonable order of magnitude.

To describe the tests with lower green densities it was necessary to let the values of f_{c0}, D_1 and n depend on the green density (Fig. 8). This is plausible since one would expect that these parameters depend on the structure of the powder compact. The reaction and transport coefficients were not changed.

In summary a relatively large set of experiments can be described with a moderate number of parameters having a clear physical meaning. This suggests that the basic ideas of the model are correct and applicable to Si_3N_4 and probably to similar systems.

Figure 9 shows the calculated densification rate for the free sintering test with hold temperature 1700°C. Also shown are the contributions of melting, rearrangement and contact flattening to the densification rate. Apparently the rearrangement term is necessary for describing the first sintering stage, but soon contact flattening becomes the dominant mechanism.

The drop of the densification rate in the later sintering stages is primarily caused by a drop of the sintering stress. Initially the main contribution to the sintering stress is the liquid pressure, which decreases, as small pores are filled and only larger and larger pores remain unfilled. However, this decrease of the liquid pressure alone would not explain the slow sintering rate at higher densities. More
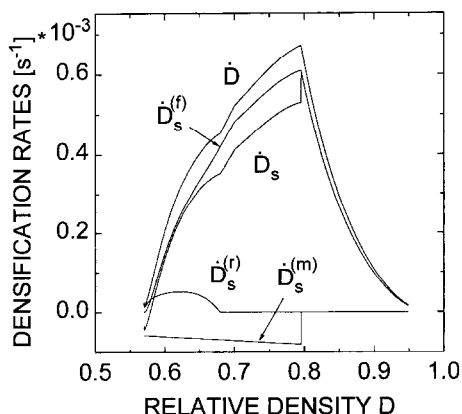
importantly, the contribution of the solid–liquid interface energy to the sintering stress is negative and its amount increases with densification. At a certain point the contribution of the solid–liquid interface energy would balance the liquid pressure and sintering would come to a standstill, if the grain size were constant. At this stage, grain coarsening becomes essential for the continuation of densification, and the coarsening rate controls the whole process. The equations quantifying these ideas are obviously successful in describing the measured densification rates.

In the literature [2–4] it was proposed that the material could densify largely without the contact flattening mechanism, solely by grain coarsening and a concomitant rearrangement of the grains. The idea is that the material of the dissolving small grains is deposited on the large grains in a way that grain shape accommodation occurs, so that the large growing grains fill the space more effectively, while the space left by the small grains is recovered by rearrangement.

This idea can be integrated in the present model by allowing the solid density achievable by rearrangement to increase as a consequence of grain shape accommodation. We calculate the achievable solid density as the solid mass in a unit cell divided by the volume of the unit cell times the achievable density in the absence of shape accommodation, D_{10}. The mass increases as $(R/R_0)^3$ by grain coarsening, while the volume decreases by contact flattening. Hence

$$D_1 = D_{10} \frac{(R/R_0)^3}{(1 - \delta)^3}. \tag{46}$$

Of course, D_1 cannot grow beyond full density and must be cut off accordingly.

However, the idea was dropped in the present work for two reasons. First, it is difficult to imagine that rearrangement is easily possible after grains have developed pronouncedly polyhedral shapes by shape accommodation. Second, the effect of equation (46) on the results was numerically insignificant in the examples presented here. In systems with more liquid phase, this kind of rearrangement could be more important, since the solid particles then have fewer and smaller contacts impeding rearrangement to a lesser extent than large contacts.

8. CONCLUSIONS

In the present model the primary densification mechanisms are particle rearrangement and contact flattening. Grain coarsening is taken into account and it plays a key role in the late sintering stages. Further, it is essential that the pore sizes are unequal with a spectrum from small to large sizes compared to the initial grain size.

The contact flattening mechanism proposed by Kingery [1] was re-analysed in greater detail including intermediate cases between pure reaction control

Fig. 9. Calculated contributions of melting, rearrangement and contact flattening to the densification rate during sintering.

and pure diffusion control. Kingery's geometrically motivated relation $c^2 = 2R^2\delta$ was shown to be asymptotically exact for small contacts, and the evolving shape of the particle near the neck is calculated (in the Appendix). Further it was shown that the analytical small-contact approximation for the contact flattening rate, equation (21), is sufficiently accurate compared to a numerical solution, even for rather large contacts. Hence the small-contact approximation is used throughout to describe contact flattening.

The complete model summarized in Section 5 is applied to tests on Si_3N_4 with very good success. A moderate number of physically meaningful adjustable parameters suffices to simulate all measured densification curves. This suggests that the most important processes are probably included in the model in an appropriate manner.

From the analysis of the tests one concludes that grain rearrangement is needed to describe the initial densification behavior. However, after only a few per cent densification, the contact flattening mechanism starts to dominate and contributes by far the greatest part to the densification in the considered system.

REFERENCES

1. W. D. Kingery, *J. appl. Phys.* **30**, 301 (1959).
2. W. J. Huppmann and G. Petzow, *Mater. Sci. Res.* **13**, 189 (1980).
3. G. Petzow and W. A. Kaysser, in *Sintered Metal-Ceramic Composites* (edited by G. S. Upadhyaya), pp. 595–614. Elsevier Science Publishers, Amsterdam (1984).
4. R. M. German, *Liquid Phase Sintering*. Plenum Press, New York (1985).
5. D. N. Yoon and W. J. Huppmann, *Acta metall.* **27**, 693 (1979).
6. H. Riedel and D. Z. Sun, in *Numerical Methods in Industrial Forming Processes, NUMIFORM '92* (edited by J. L. Chenot, R. D. Wood and O. C. Zienkiewicz), pp. 883–886. A. A. Balkema, Rotterdam (1992).
7. K. Mori, in *Numerical Methods in Industrial Forming Processes, NUMIFORM '92* (edited by J. L. Chenot, R. D. Wood and O. C. Zienkiewicz), pp. 69–78. A. A. Balkema, Rotterdam (1992).
8. D. Z. Sun and H. Riedel, in *Simulation of Materials Processing: Theory, Methods and Applications, NUMIFORM '95* (edited by S.-F. Shen and P. R. Dawson), pp. 881–886. A. A. Balkema, Rotterdam (1995).
9. S. J. L. Kang, W. A. Kaysser, G. Petzow and D. N. Yoon, *Powder Met.* **27**, 97 (1984).
10. H.-H. Park, S.-J. Cho and D. N. Yoon, *Metall. Trans.* **15A**, 1075 (1984).
11. S.-J. L. Kang, K.-H. Kim and D. N. Yoon, *J. Amer. Ceram. Soc.* **74**, 425 (1991).
12. D. R. Clarke, *J. Am. Ceram. Soc.* **70**, 15 (1987).
13. G. H. Gessinger, H. F. Fischmeister and H. L. Lukas, *Acta. metall.* **21**, 715 (1973).
14. T. H. Courtney, *Metall. Trans. A*, **8A**, 671 (1977).
15. O. H. Kwon and G. L. Messing, *Acta metall. mater.* **39**, 2059 (1991).
16. W. C. Carter, *Acta metall.* **36**, 2283 (1988).
17. J. Svoboda and H. Riedel, *Acta metall. mater.* **43**, 1 (1995).
18. W. J. Huppmann, H. Riegger and G. Petzow, *Sci. Sintering* **10**, 45 (1978).
19. Z. S. Nikolic and W. J. Huppmann, *Acta metall.* **28**, 475 (1980).
20. J. Svoboda and H. Riedel, *Acta metall. mater.* **40**, 2829 (1992).
21. J. Svoboda, H. Riedel and H. Zipse, *Acta metall. mater.* **42**, 435 (1994).
22. D.-D. Lee, S.-J. L. Kang and D. N. Yoon, *J. Am. Ceram. Soc.* **71**, 803 (1988).
23. E. Arzt, *Acta metall.* **30**, 1883 (1982).
24. A. S. Helle, K. E. Easterling and M. F. Ashby, *Acta metall.* **33**, 2163 (1985).
25. R. K. Venkatachari and R. Raj, *J. Am. Ceram. Soc.* **69**, 499 (1986).
26. H. Zipse and H. Riedel, in *Ceramic Transactions, Vol. 51: Ceramic Processing and Technology* (edited by H. Hausner, G. L. Messing and S.-i. Hirano), pp. 489–493. American Ceramic Society, Westerville, (1995).
27. R. Gaebel, PhD thesis, University of Karlsruhe, (1996).

APPENDIX

Shape of the Solid–Liquid Interface

When initially spherical particles approach one another to form a contact, the particle shape cannot remain exactly spherical, since the dihedral angle at the edge of the contact must be zero for a fully wetting liquid. It will be shown, however, that the disturbance remains small, and is confined to a small zone, as long as $c \ll R$. Far away from the contact the particle is still spherical with radius R. We denote the deviation of the particle surface from the sphere by $y(s)$, so that $R - y(s)$ is the distance of a point on the solid–liquid interface from the center of the sphere.

Equations (8), (10) and (11) determine the evolution of the solid–liquid interface. For short times, or small contacts, these equations can be linearized in terms of y to yield

$$\dot{y} + \gamma_{sl}\Omega L y'' = 0. \tag{A1}$$

Here the curvature was calculated neglecting y/R and y'^2 compared to 1, which is justified for short times. The prime denotes the derivative with respect to the arc length s measured from the center of the contact. (In the linear approximation $s = r$.)

We seek a solution of the partial differential equation (A1) for the case of a growing contact with radius $c(t)$; the dihedral angle at the edge of the contact must be zero. This implies $y'(c) = -c/R$. In analogy to neck formation in solid-state sintering [17] one solves the problem by trying similarity solutions of the form

$$y = R\left(\frac{c}{R}\right)^\beta Y(S) \tag{A2}$$

with the coordinate

$$S = \frac{s - c}{R}\left(\frac{R}{c}\right)^\alpha \tag{A3}$$

where $c(t)$, α and β are as yet unspecified. In calculating the time derivative of y, one exploits the conjecture to be verified later that the disturbance is not only small but is also confined to a small zone whose size can be neglected compared to c (cf. [17]).

The similarity solution reduces the partial differential

equation (A1) to two ordinary differential equations for $c(t)$ and $Y(S)$, which can be solved readily:

$$\left(\frac{c}{R}\right)^{\alpha+1} = (\alpha + 1)\frac{\gamma_{sl}\Omega L}{\lambda R^2}\, t \qquad (A4)$$

$$Y = \lambda e^{-S/\lambda}, \qquad (A5)$$

where λ is an as yet unspecified dimensionless factor, which plays the role of a (dimensionless) characteristic length in equation (A5). Equation (A5) fulfils the boundary conditions $Y(\infty) = 0$ and $Y'(0) = -1$, which guarantees that the dihedral angle is zero. This condition also specifies $\beta = \alpha + 1$.

Further, $y(c)$ must compensate the particle displacement and growth, so that the contact edge stays in the symmetry plane between the two particles. This means

$$y(c) = R\delta + (R - R_0) - \frac{c^2}{2R}. \qquad (A6)$$

It turns out that $R\delta$ and $c^2/(2R)$ are the leading terms in this equation, since they increase as $t^{2/(\alpha+1)}$ (with $\alpha > 1$ as we shall see), while $y(c)$ and $R - R_0$ are linear in t. Hence the relation $c^2 = 2R^2\delta$, equation (27), is asymptotically exact for small t.

Finally, α and λ are specified by a comparison of equation (A4) with equation (28) with δ replaced by $c^2/(2R^2)$. In the reaction controlled limit one obtains $\alpha = 3$, $\beta = 4$, and

$$\lambda = \frac{ZD_s\gamma_{sl}}{4R(\sigma_1 - \sigma_m)}. \qquad (A7)$$

For $\sigma_m = 0$ and $Z = 8$ is $\lambda \approx 0.5$. In the diffusion controlled limit one finds $\alpha = 5$, $\beta = 6$, and

$$\lambda = \frac{ZD_s kTL\gamma_{sl}R}{16C_1\delta_b D_b(\sigma_1 - \sigma_m)}. \qquad (A8)$$

Now the profile of the solid–liquid interface and its evolution are completely specified by equations (A2), (A5) and (A7) or (A8). This solution is valid as long as the characteristic length of the disturbance is small compared to c

$$c\left(\frac{c}{R}\right)^{\alpha-1}\lambda \ll c. \qquad (A9)$$

This condition is readily fulfilled in the reaction controlled limit even for c/R as large as 0.4. As a consequence the analytical and numerical results for the surface profile, equation (A5) and Fig. 2(a), are consistent. In the diffusion controlled limit, however, λ may be large (when D_b/L is small), so that equation (A9) starts to be violated already at smaller c/R. This means that the disturbance of the spherical shape spreads over the entire sphere, and the solid–liquid interface approaches an equilibrium shape with constant mean curvature. However, in the diffusion dominated cases shown in Figs 2(b), 3 and 4 the small-contact relation, $c^2 = 2R^2\delta$, is still approximately valid, since with the diffusion coefficients assumed in the figures equation (A9) is violated only when $c/R \approx 0.32$. Correspondingly the numerical results confirm the small-contact approximation. For even slower diffusion, the validity of the small-contact approximation is more restricted. One could then consider using the (numerical) equilibrium solutions for the contact radius developed in Ref. [21]. In this investigation a linear, rather than a parabolic, relation between c and δ was obtained: $c/R \approx 5.5\delta$ (for $\psi = 0$).